Delicate Lattice Modulation Enables Superior Na Storage Performance of $Na_3V_2(PO_4)_3$ as Both Anode and Cathode Materials for Sodium-Ion Batteries: Understanding the Role of Calcium Substitution for Vanadium

Lina Zhao,[a] Hailei Zhao,[*ab] Zhihong Du,[ab] Jie Wang,[ab], Xuanyou Long[a], Zhaolin Li,[a] Konrad Świerczek[c]

[a] School of Materials Science and Engineering, University of Science and Technology Beijing, Beijing 100083, China

[b] Beijing Municipal Key Laboratory of New Energy Materials and Technologies, Beijing 100083, China

[c] AGH University of Science and Technology, Faculty of Energy and Fuels, Department of Hydrogen Energy, al. A. Mickiewicza 30, 30-059 Krakow, Poland

[*]Corresponding author:

E-mail address: hlzhao@ustb.edu.cn

Experimental Section

Synthesis: $Na_3V_{2-x}Ca_x(PO_4)_3$@C (x = 0, 0.05 and 0.10) composites were prepared using solvothermal-assisted reaction with post calcination. First, stoichiometric amounts of V_2O_5 (0.3 M), $Ca(NO_3)_2$, NaH_2PO_4, oxalic acid and citric acid were dissolved in deionized (DI) water at 80 °C. 10 ml of the obtained solution was added into ethylene glycol (50 ml) and kept vigorously stirred for 2 h. Then, the mixture was transferred to a 100 ml Teflon-lined stainless-steel autoclave and kept in an oven at 200 °C for 12 h. The resulting precursor solution was dried in oven at 120 °C in air. Finally, the obtained solid precursor was ground in a mortar and further annealed in a tube furnace at 650 °C for 6 h under Ar flow. During the final step, the desired crystal structure of $Na_3V_{2-x}Ca_x(PO_4)_3$ was formed, as well as the organic components underwent decomposition, resulting in a formation of uniformly-distributed carbon layer.

Characterization of materials: Crystallographic phases of all the products were investigated by powder X-ray diffraction (Rigaku, D/max-A, Cu-K_α, λ = 1.5406 Å). The Rietveld method was applied to refine the recorded XRD patterns using the General Structure Analysis System (GSAS) with the EXPGUI graphical user interface[1]. Morphology and microstructure of the samples were examined by field-emission scanning electron microscopy (FE-SEM, SUPRA55) and transmission electron microscopy (TEM, FEI/Tecnai G2 F20 S-TWIN TMP, 200 kV). Inductive couple plasma optical emission spectrometer (ICP-OES) analysis was performed using an Agilent S730 to identify the chemical compositions. The oxidation states of the elements were examined by X-ray photoelectron spectroscopy (XPS, Thermo escalab 250XI, Al Kα, hν = 1486.6 eV). The spectrometer was calibrated with respect to the C 1s peak binding energy of 284.6 eV. The carbon content in the composites was measured by thermogravimetric analysis (TGA, TA Q5000 IR) with a heating rate of 10 °C min^{-1} from room temperature to 700 °C in air. Raman spectra were recorded using Raman microscopy system (Renishaw, RM 2000, Britain) at a laser wavelength of 632.8 nm.

Electrochemical Measurements: The working electrode slurry was prepared by dispersing $Na_3V_{2-x}Ca_x(PO_4)_3$@C, acetylene black and poly-(vinylidene fluoride) (PVDF) binder in an N-methyl pyrrolidone (NMP) solution at a weight ratio of 70:15:15. The slurry was spread on aluminum (positive electrode)/copper (negative electrode) foil and dried in a vacuum oven at 120 °C for 10 h prior to 2032 coin cells assembly. The typical loading mass of cathode material in electrode film is around 2-4 mg cm^{-2}. Sodium foil was used as the counter electrode, 1.0 M $NaClO_4$ in ethyl carbonate (EC)/dimethyl carbonate (DMC) (1:1 v/v ratio) with 5 vol% fluoroethylene carbonate (FEC) was used as the electrolyte and glass fiber filter (Whatman GF/A) was the separator. Galvanostatic charging/discharging was conducted on a multichannel battery testing system (LAND CT-2001A) in the ranges of 2.0-4.3 V for the cathodic reaction and 0.01-2.5 V for the anodic reaction. Cyclic voltammetry measurements were performed on Arbin instruments device (Model BT 2000). Electrochemical impedance spectra (EIS) were recorded in a frequency range from 10^6 to 0.01 Hz, while the disturbance amplitude was 10 mV. For symmetric NVP sodium ion battery tests, the cells were assembled as coin-type full cells with $Na_3V_{1.95}Ca_{0.05}(PO_4)_3$@C-based layers used as both cathode and anode. Capacity balance of the full cells was achieved by setting the mass ratio of cathode/anode to 1.5. Charge/discharge measurements for the full cells were carried out between 1.0 V and 4.0 V.

Density Functional Theory (DFT) calculations: The first-principles DFT calculations were carried out to investigate the Ca doping effects on NVP materials using Cambridge Serial Total Energy Package (CASTEP) function implemented in Materials Studio (MS) software. The exchange-correlation parameterization was described with spin-polarized generalized gradient approximation (GGA) and the Perdew-Burke-Ernzerhof (PBE) fuctional. The plane-wave basis set was determined with a cutoff energy of 520 eV and the *k*-point sampling of Brillouin-zone integrals using a 3×3×3 Gamma grid. The convergence condition of the residual force was set at 2×10^{-6} eV $atom^{-1}$. Hubbard

U parameter (GGA+U) was used to correct the incomplete cancellation of the self-interaction of GGA. The U value was set to 4.0 eV for vanadium atoms, whereas the correction was not used for other elements[2,3]. The calculations were performed in a rhombohedral supercell consisting of 4 formula units of $Na_3V_2(PO_4)_3$. The Na vacancy arrangement with the lowest energy was selected, which had been demonstrated previously in the literature[4,5]. The chemical formula with Ca doping amount x = 0.25 was chosen to simplify the calculation process. The transition state search (TS Search) method was implemented to calculate the migration energy for possible diffusion pathways of sodium ions. The lattice energy was determined by equation (1)[6,7]:

$$E_{lattice} = \frac{E(M) - \sum E(atom)}{n} \quad (1)$$

where *E(M)* represents the total energy of the model structure, *E(atom)* is the total energy of all atoms used in the model, and *n* represents the number of the unit cell involved in the structural model.

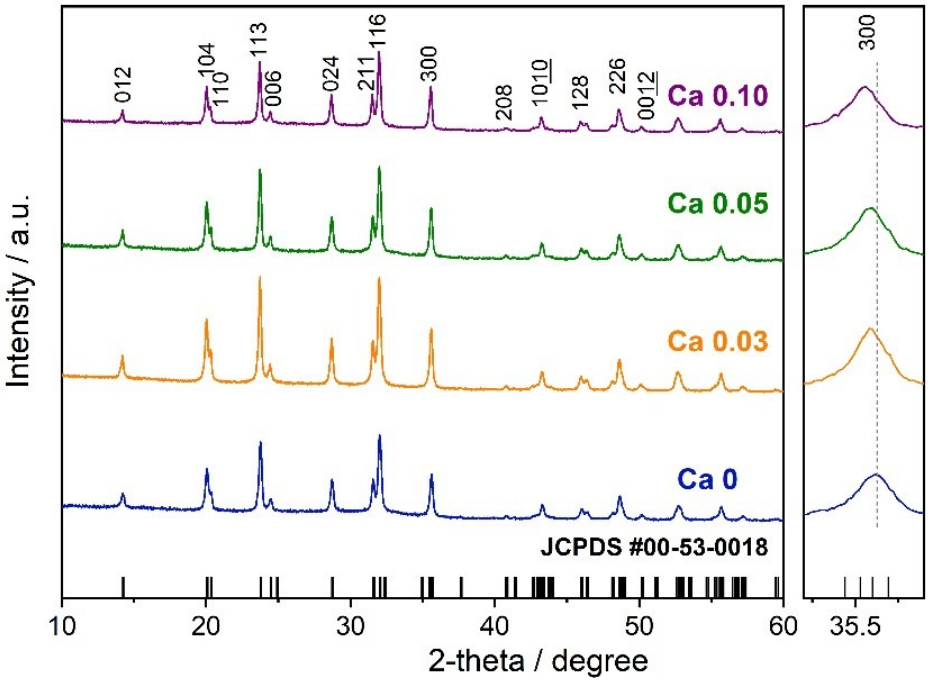

Fig. S1. XRD patterns of $Na_3V_{2-x}Ca_x(PO_4)_3$@C (x = 0, 0.03, 0.05, 0.10) materials.

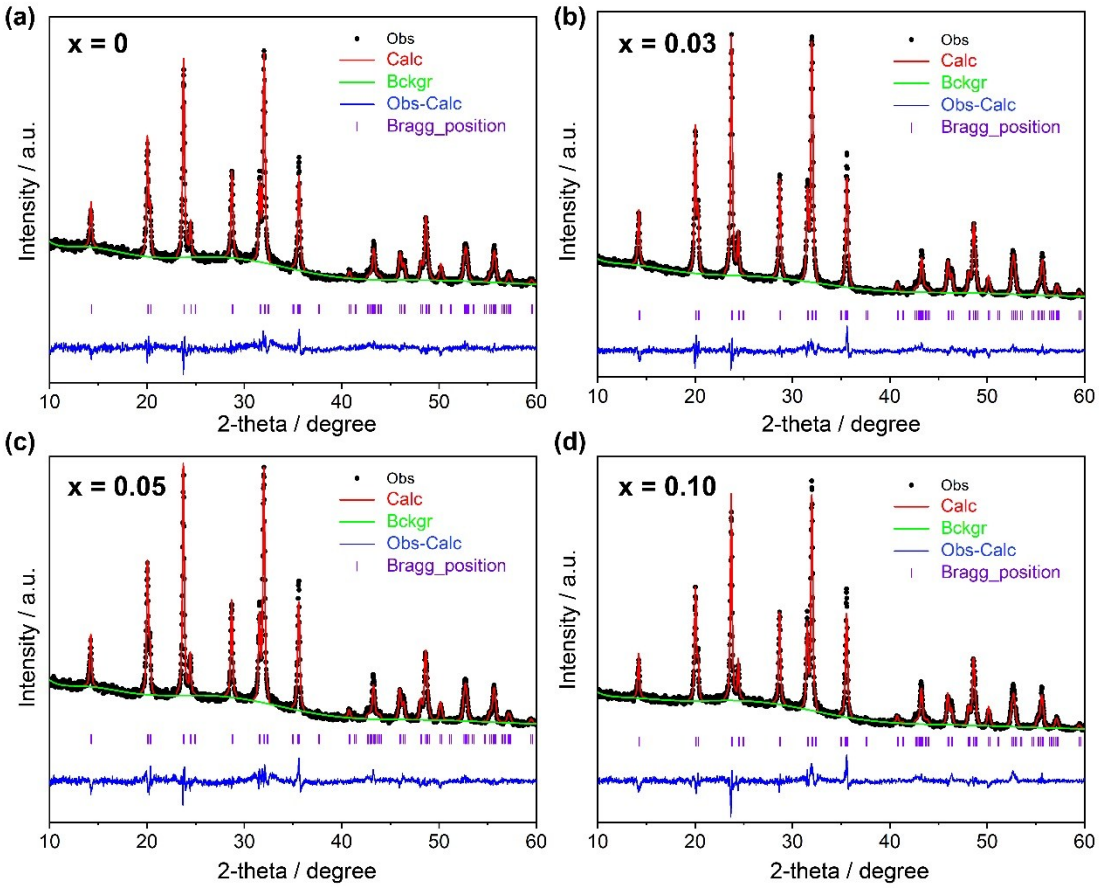

Fig. S2. Rietveld refinements of structural data recorded for $Na_3V_2(PO_4)_3$ (a), $Na_3V_{1.97}Ca_{0.03}(PO_4)_3$ (b), $Na_3V_{1.95}Ca_{0.05}(PO_4)_3$ (c) and $Na_3V_{1.90}Ca_{0.10}(PO_4)_3$ (d) at RT. The black points show the observed intensities. The red solid line and green solid line represent calculated and background lines, respectively. The blue curve demonstrates difference between the observed and the calculated intensities. Violet vertical bars indicate positions of Bragg reflections for $R\bar{3}c$ space group.

Table S1. Refined structural parameters of $Na_3V_{2-x}Ca_x(PO_4)_3$ (x = 0, 0.03, 0.05, 0.10) samples.

	x = 0	x = 0.03	x = 0.05	x = 0.10
Unit cell parameter *a* (=*b*) [Å]	8.7319(3)	8.7341(4)	8.7354(7)	8.7391(4)
Unit cell parameter *c* [Å]	21.834(1)	21.827(1)	21.824(2)	21.817(1)
Unit cell volume *v* [Å]	1441.7(1)	1441.8(2)	1442.4(3)	1443.2(2)
Na(1) occupancy	0.91(2)	0.88(4)	0.87(3)	0.86(2)
Na(2) occupancy	0.696(5)	0.709(1)	0.710(2)	0.712(7)
R*wp* [%]	6.66	5.65	6.75	7.41
χ^2	1.620	1.183	1.716	2.121

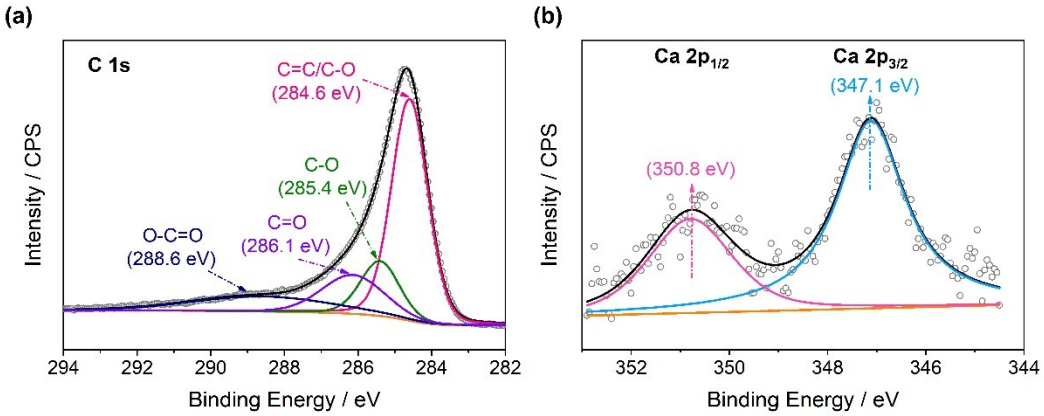

Fig. S3. XPS spectra with deconvoluted C 1s peaks (a) and Ca 2p peaks (b) recorded for $Na_3V_{1.90}Ca_{0.10}(PO_4)_3$@C sample.

As displayed in Figure S3, C1s spectrum can be fitted with four peaks, which correspond to C-relevant functional groups, proving the existence of carbon in the investigated sample. Ca 2p XPS spectra of $Na_3V_{1.90}Ca_{0.10}(PO_4)_3$ consists of two broad bands at 350.8 eV and 347.1 eV, which correspond to Ca $2p_{1/2}$ and $2p_{3/2}$ transitions, respectively, further confirming the presence of Ca^{2+} in $Na_3V_{1.90}Ca_{0.10}(PO_4)_3$@C sample[8,9].

Table S2. XPS fitting results for $V2p_{3/2}$ signals in $Na_3V_{1.90}Ca_{0.10}(PO_4)_3$ sample.

	Binding Energy / eV	FWHM / eV	Area / eV cps
$V^{3+}2p_{3/2}$	516.9	2.15	23506.585
$V^{4+}2p_{3/2}$	517.6	1.06	1304.472

Table S3. Molar ratios of of Na, V, P and Ca in $Na_3V_{1.95}Ca_{0.05}(PO_4)_3$ and $Na_3V_2(PO_4)_3$ samples determined by ICP-OES.

Na:V:Ca:P	x=0	x=0.05
theroretical	3:2:3	3:1.95:0.05:3
experimental	2.95:2.02:3	2.96:1.96:0.06:3

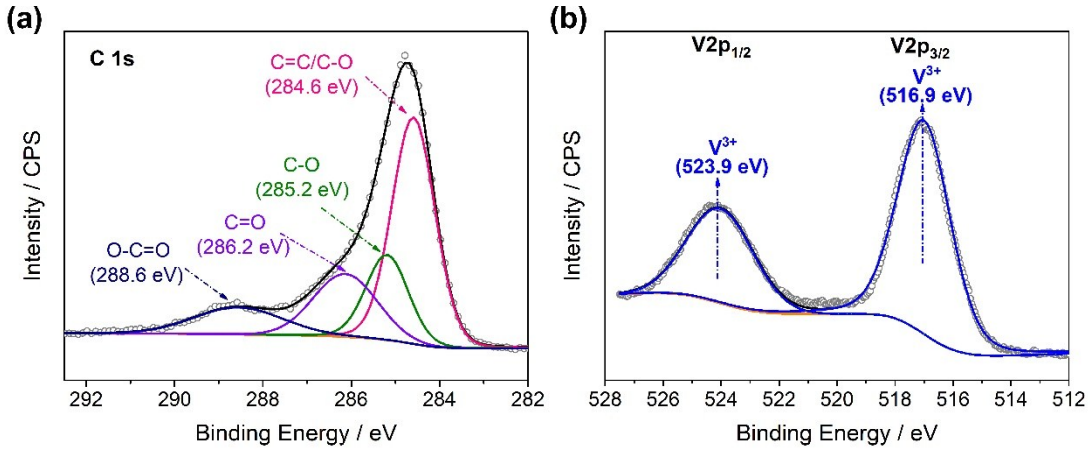

Fig. S4. XPS spectra of C 1s (a) and V 2p (b) for bare $Na_3V_2(PO_4)_3$.

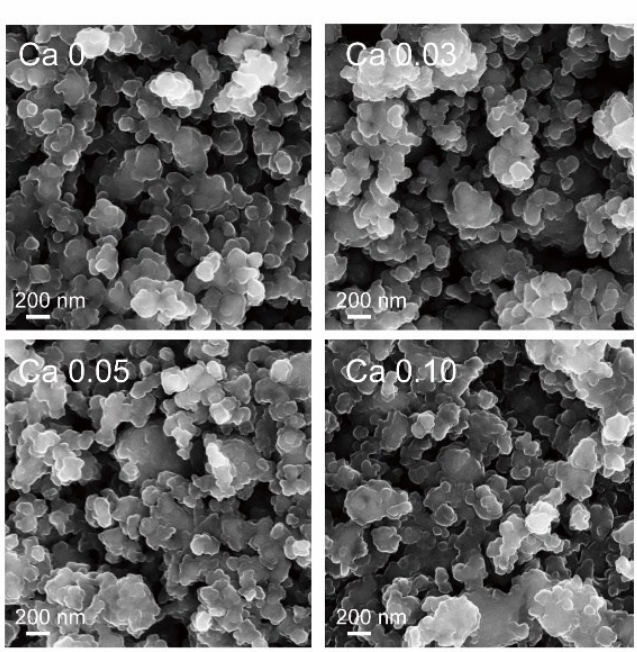

Fig. S5. FE-SEM micrographs of $Na_3V_{2-x}Ca_x(PO_4)_3$ (x = 0, 0.03, 0.05, 0.10) materials.

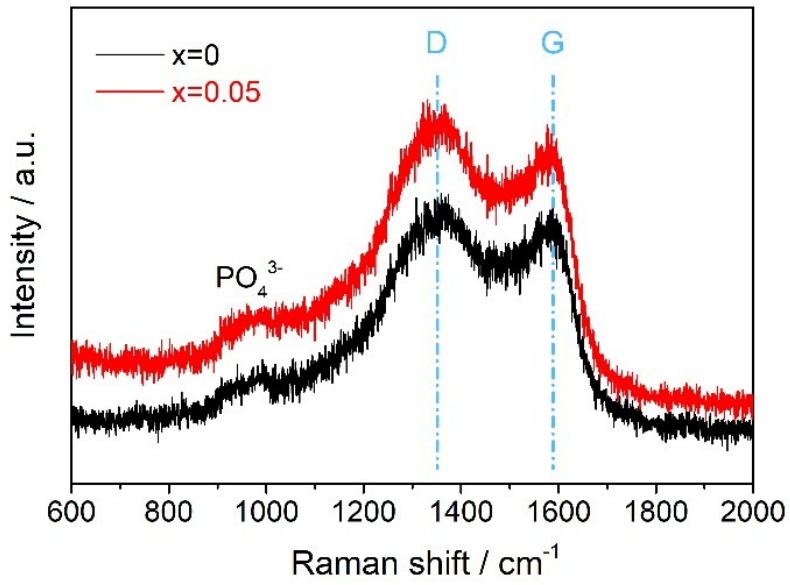

Fig. S6. Raman spectra of $Na_3V_2(PO_4)_3$@C and $Na_3V_{1.95}Ca_{0.05}(PO_4)_3$@C samples.

Two broad, characteristic peaks located at 1350 and 1588 cm^{-1} are attributed to the D (disordered carbon, sp^3-cooridinated behavior) and G (crystalline graphitized carbon, sp^2-coordinated behavior) bands, which can be assigned to the amorphous carbon layer formed during the final annealing process. Additional peaks visible at around 1000 cm^{-1} can attributed to the stretching vibration of PO_4 [10]. The peak intensity ratio (I_D/I_G) was calculated to be 1.08 for both samples, indicating a high degree of graphitization of the carbon layer. Consequently, high electric conductivity may be expected.

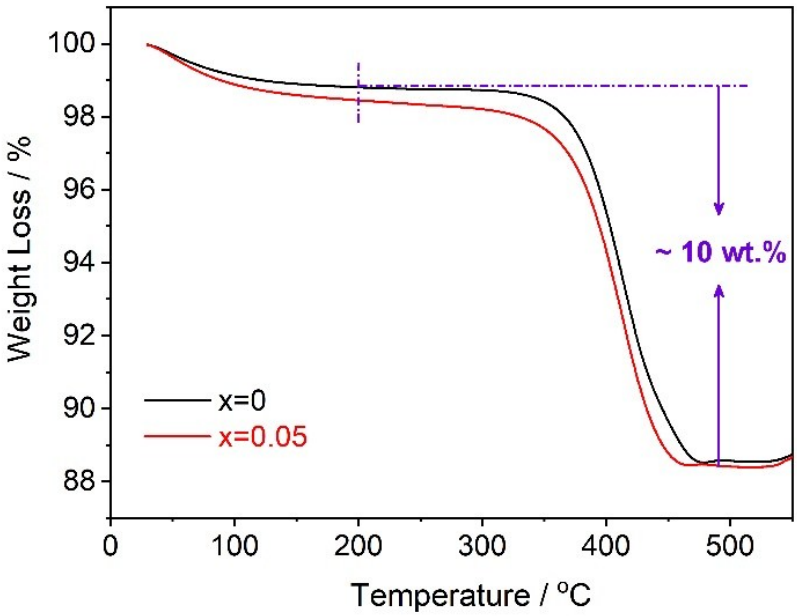

Fig. S7. TG curves of $Na_3V_2(PO_4)_3$@C and $Na_3V_{1.95}Ca_{0.05}(PO_4)_3$@C samples recorded in air.

The initial loss (up to 200 °C) can be attributed to desorption of surface-adsorbed species and was not taken into account during evaluation of the carbon content.

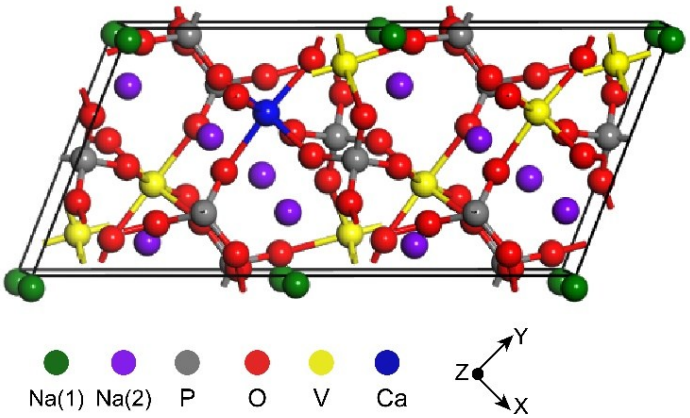

Fig. S8. Visualization of the unit cell of $Na_3V_{1.75}Ca_{0.25}(PO_4)_3$ for calculation.

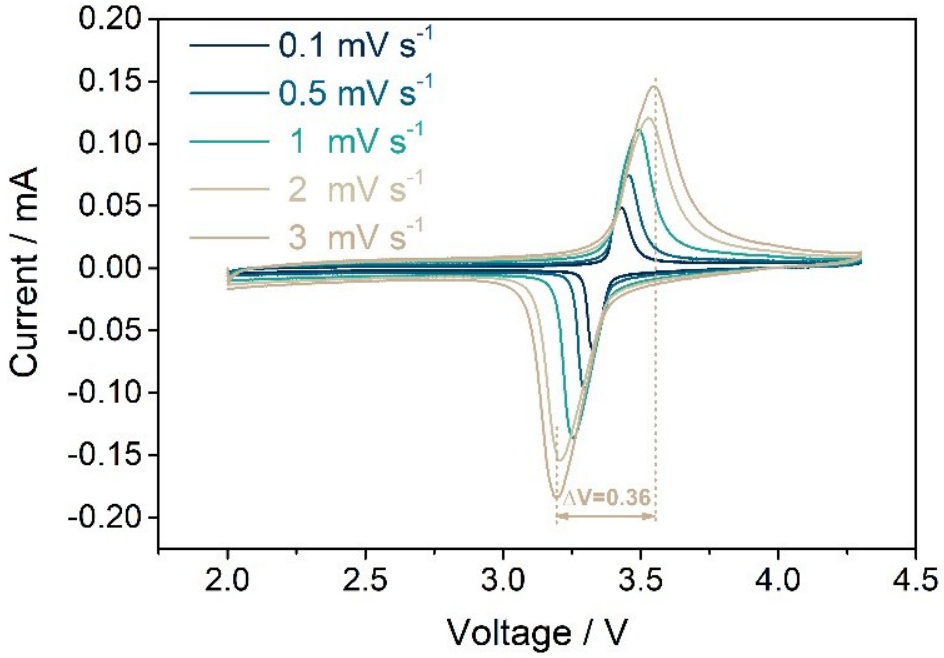

Fig. S9. CV curves for $Na_3V_2(PO_4)_3$@C electrode recorded in the voltage range of 2.0-4.3 V at various scan rates from 0.1 mV s^{-1} to 3 mV s^{-1}.

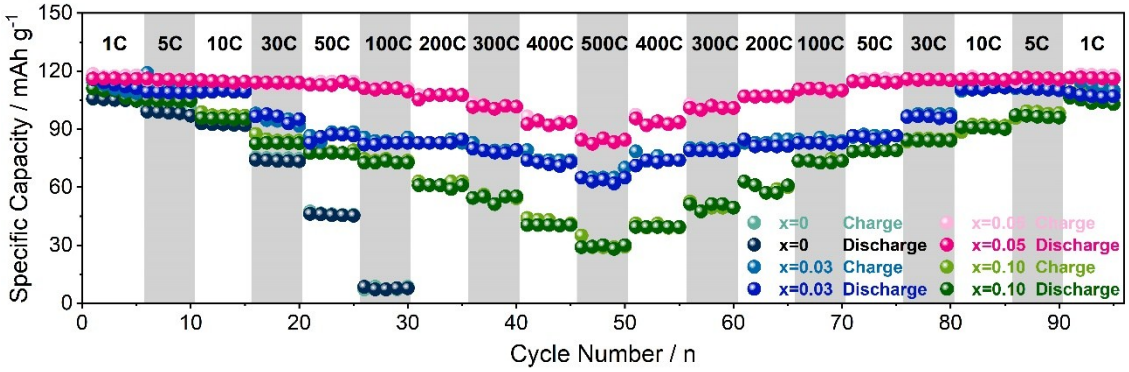

Fig. S10. Rate capability of the prepared $Na_3V_{2-x}Ca_x(PO_4)_3$ (x = 0, 0.03, 0.05, 0.10) electrodes as cathode materials.

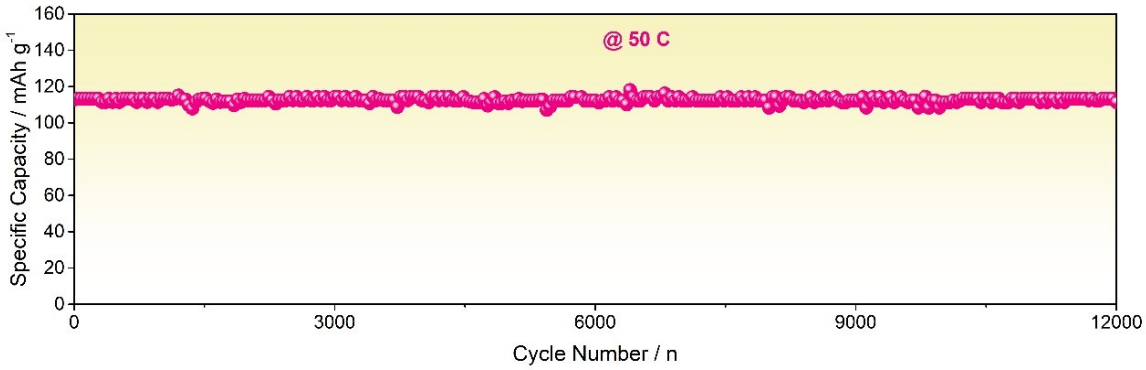

Fig. S11. Long-term cycling performance of $Na_3V_{1.95}Ca_{0.05}(PO_4)_3$@C cathode recorded at a high current rate of 50 C over 12000 cycles.

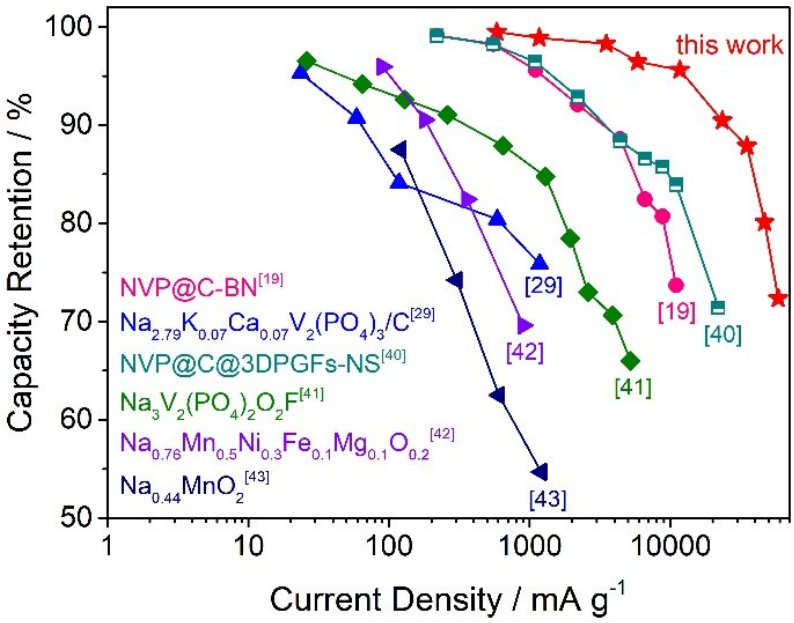

Fig. S12. Comparison of the rate performance of the $Na_3V_{1.95}Ca_{0.05}(PO_4)_3$@C cathode in this work with recently reported $Na_3V_2(PO_4)_3$ cathode materials and currently considered cathode material candidates for SIBs.

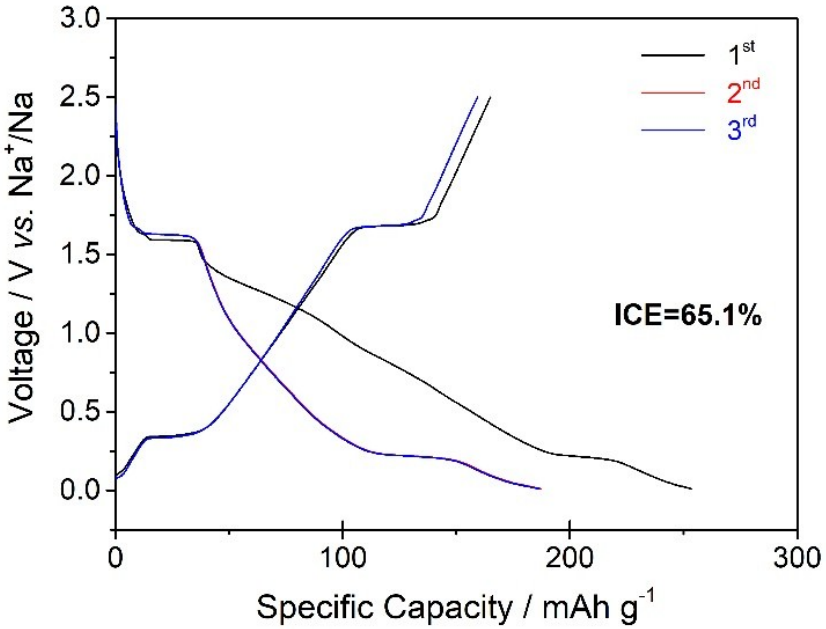

Fig. S13. Galvanostatic charge/discharge profiles of $Na_3V_{1.95}Ca_{0.05}(PO_4)_3$@C anode at 0.1 C for the first three cycles.

Three typical voltage plateaus of $Na_3V_{1.95}Ca_{0.05}(PO_4)_3$@C anode match well with the results observed in CV curves. The flat discharge plateaus at ~1.6 V and 0.3 V correspond to two stepwise insertion processes of two Na ions. The initial, measured discharge capacity is 253.4 mAh g^{-1} and the reversible charge capacity is 165 mAh g^{-1}, corresponding to 65.1% of the initial Coulombic efficiency. The excessive capacity can be attributed to the coating carbon shell (~30 mAh g^{-1}) and the carbonaceous additives (~20 mAh g^{-1}).

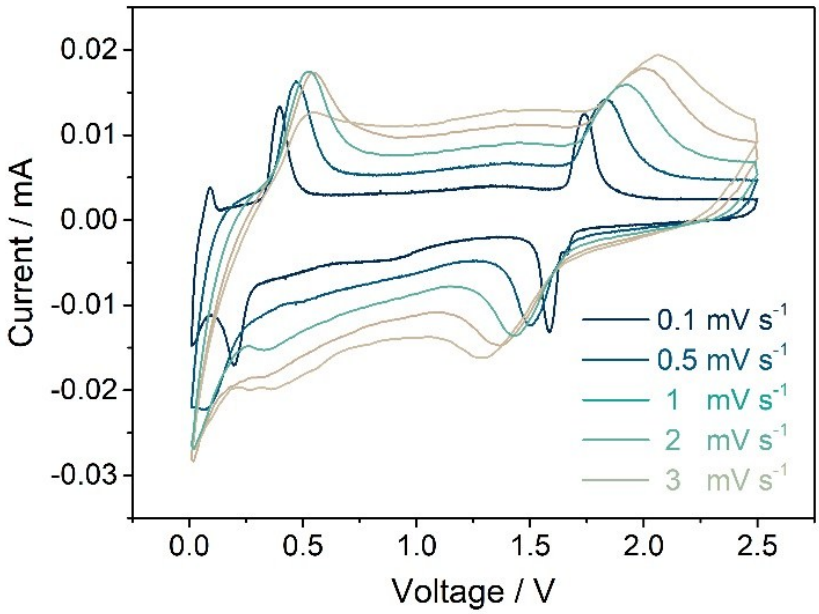

Fig. S14. CV curves of $Na_3V_2(PO_4)_3$@C electrode measured at various scan rates from 0.1 V to 3 mV s^{-1} between 0.01-2.5 V.

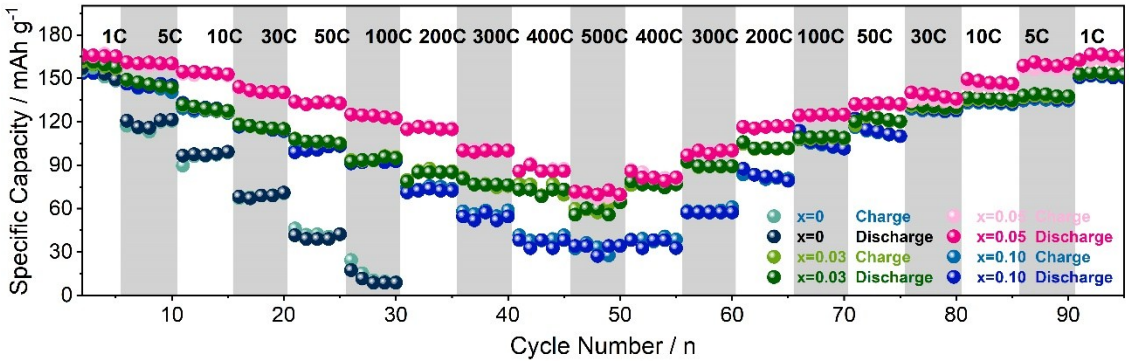

Fig. S15. Rate capability of the $Na_3V_{2-x}Ca_x(PO_4)_3$ (x = 0, 0.03, 0.05, 0.10) electrodes as anode materials.

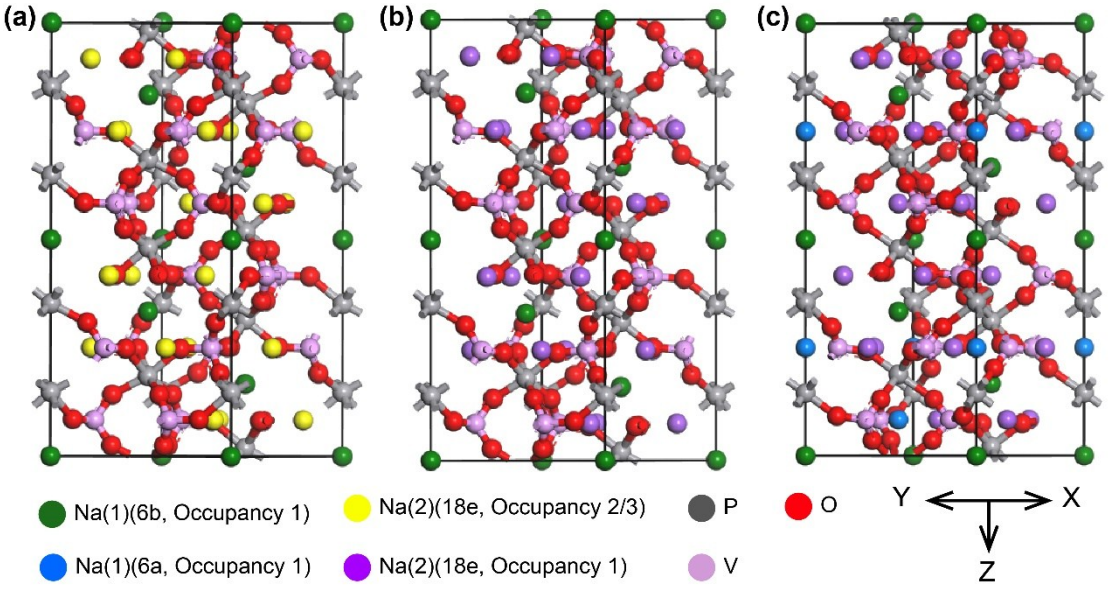

Fig. S16. Visualization of the unit cell of (a) $Na_3V_2(PO_4)_3$, (b) $Na_4V_2(PO_4)_3$ and (c) $Na_5V_2(PO_4)_3$ for calculations.

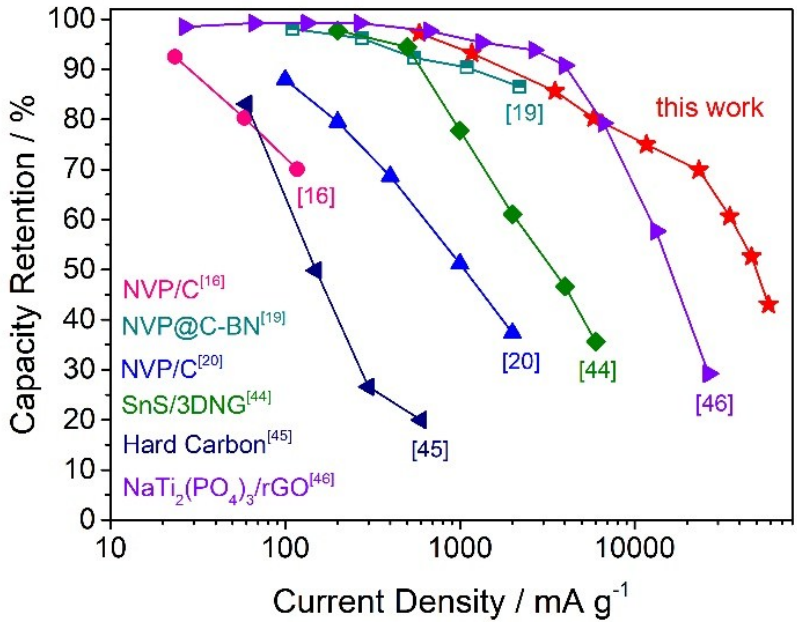

Fig. S17. Comparison of the rate performance of the $Na_3V_{1.95}Ca_{0.05}(PO_4)_3$@C anode in this work with recently reported $Na_3V_2(PO_4)_3$ anode materials and currently considered anode material candidates for SIBs.

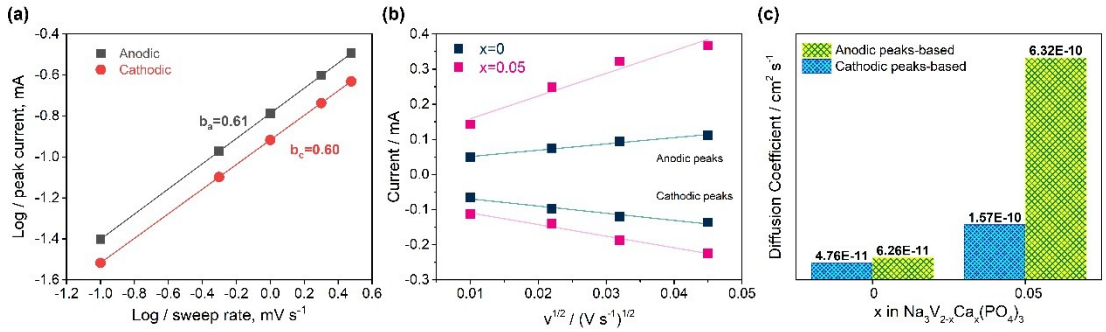

Fig. S18. Analysis of the reaction kinetics when NVP was applied as cathode for NIBs: (a) Relationship between logarithm anodic/cathodic peak current and logarithm scan rates of $Na_3V_{1.95}Ca_{0.05}(PO_4)_3$@C cathode; (b) The linear fitting between the peak current and the square root of the scan rate; (c) Sodium ion diffusion coefficients.

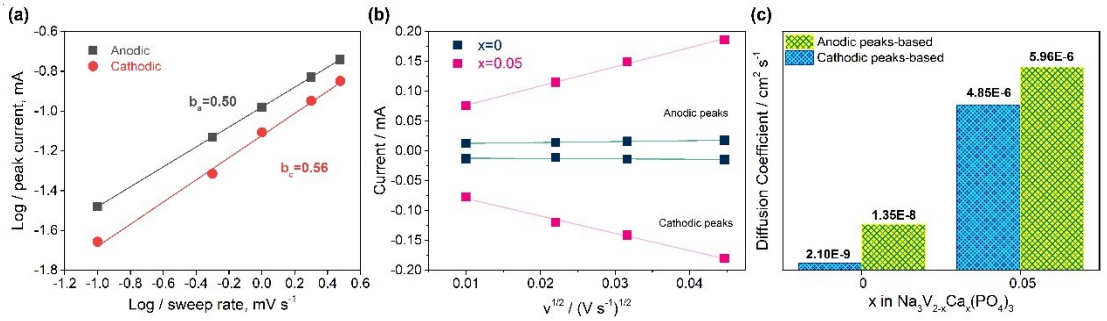

Fig. S19. Analysis of the reaction kinetics when NVP was applied as anode for NIBs: (a) Relationship between logarithm anodic/cathodic peak current and logarithm scan rates of $Na_3V_{1.95}Ca_{0.05}(PO_4)_3$@C anode; (b) The linear fitting between the peak current and the square root of the scan rate; (c) Sodium ion diffusion coefficients.

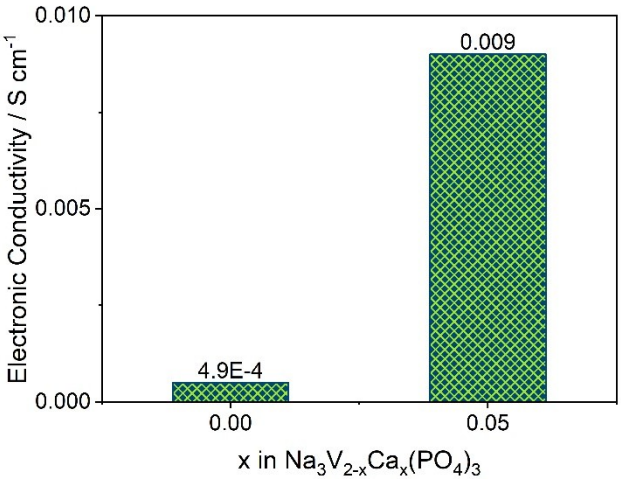

Fig. S20. Electronic conductivity measured by RST-4 linear four-point probe method.

References

[1] A. C. Larson, R. B. Von Dreele, *Generalized structure analysis system (GSAS). Laur 86-748*, Los Alamos National Laboratory, Los Alamos, **1994**.

[2] Q. Kuang, Z. Lin, Y. Zhao, X. Chen and L. Chen, *J. Mater. Chem.* **2011,** 21, 14760.

[3] S. Y. Lim, H. Kim, R. A. Shakoor, Y. Jung and J. W. Choi, *J. Electrochem. Soc.* **2012**, 159, 1393.

[4] H. Kabbour, D. Coillot, M. Colmont, C. Masquelier and O. Mentre, *J. Am. Chem. Soc.* **2011**, 133, 11900.

[5] J. N. Chotard, G. Rousse, R. David, O. Mentré, M. Courty and C. Masquelier, *Chem. Mater.* **2015**, 27, 5982-5987.

[6] Y. Liao, K.-S. Park, P. Xiao, G. Henkelman, W. Li and J. B. Goodenough, *Chem. Mater.* **2013**, 25, 1699.

[7] R. Pushpa, D. Daniel and D. P. Butt, *Solid State Ion.* **2013**, 249, 184.

[8] S. Wang, Y. Chen, S. Fang, L. Zhang, M. Tang, K. An, K. S. Brinkman and F. Chen, *Chem. Mater.* **2014**, 26, 2021.

[9] A. Dutta, S. Saha, P. Kumari, T. P. Sinha and S. Shannigrahi, *J. Solid State Chem.* **2015**, 229, 296.

[10] Z. Jian, W. Han , X. Lu , H. Yang , Y. Hu , J. Zhou , Z. Zhou , J. Li , W. Chen, D. Chen , L. Chen , *Adv. Energy Mater.* **2013**, *3*, 156.